

Reproducing the Hong-Ou-Mandel dip using bulk optics

Andrés Ducuara, Lana Mineh, Ben Sayers,
John Scott, Dominic Sulway, Oliver Thomas

Cohort 4
Quantum Engineering CDT
University of Bristol

January 19, 2018

Abstract

A Hong-Ou-Mandel dip with a ratio of coincidences/singles of 2.3% and coincidence/accidentals of 26.1 is presented here. A visibility of $91.9 \pm 0.5\%$ was achieved using a 2.5 ns time window demonstrating a quantum interference effect. A detailed description of the bulk optical setup used is given.

1 Introduction

Hong-Ou-Mandel (HOM) interference is a unique quantum mechanical effect which was first discovered in 1987 [1]. This effect occurs when pairs of photons with varying levels of distinguishability interfere on a beam splitter. Coincident photons are measured by two detectors directed at each output port of the beam splitter causing a coincidence count between both detectors. These coincidence counts can be altered by varying a degree of freedom (such as displacement of the optical path) of one of the photons sent into the beam splitter. If the photons are identical they destructively interfere, leaving zero coincidences, which accounts for the HOM dip.

This effect is vital to the operation of optical quantum technologies such as quantum computing [2] and has been demonstrated in bulk optic [3], fibre optic [4] and integrated optic arrangements [5]. It was also shown in the original publication [1] that this method of interference may be used to measure the duration of a pulse of light and, as other publications have noted, can be used to assess the purity of

states of light [6]. Bulk optical elements have been used for this experiment as they can be reconfigured and individually optimised to the needs of the experiment.

Visibility quantifies how well an interferometer can measure coherence between two optical fields. A higher visibility is essential in HOM interference to accurately measure photon path lengths and timing, and hence is directly related to the fidelity of optical quantum gates. Demonstration of the HOM effect in our own experiment would allow further investigation into the limits of calculating the width of the observed dip in coincidences as well as observing ways to optimise visibility.

In this report we begin by introducing the theory necessary to understand HOM interference and its associated dip. We then outline the experimental methods and equipment used to obtain the dip in coincidence counts using bulk optical elements. We then present results of these methods and analyse our experiment in detail. Finally, we discuss areas of our method which require improvement and suggest

strategies to mitigate problems in future iterations of this experiment.

2 Theoretical Model

In this section, we start by describing the quantum state of a pair of photons generated by the process known as Spontaneous Parametric Down Conversion (SPDC). This process is particularly useful for this experiment because it leads to highly indistinguishable pairs of photons. We then consider the state transformation introduced by a delay in one of the paths taken by the photons followed by a 50:50 beam splitter. We end up by calculating the probability of obtaining coincidences in detectors positioned at the outputs of the beam splitter, which is a function of the introduced path delay. We show that this function presents a “dip” when approaching zero-delay and show how different profiles of the down converted photons lead to different shapes of the dips.

2.1 Spontaneous Parametric Down Conversion

The process of SPDC refers to the situation when a photon (pump) with frequency ω_p and wave vector \mathbf{k}_p goes through a nonlinear crystal. This produces two daughter photons a and b (also called signal and idler photons) with respective frequencies ω_a, ω_b and wave vectors $\mathbf{k}_a, \mathbf{k}_b$, leaving the nonlinear crystal at opposite sides of a cone with a particular angle that depends on the properties of the crystal [Fig. 1](#). Due to conservation of energy and momentum, these quantities should satisfy the relationships:

$$\omega_p = \omega_a + \omega_b \quad (1a)$$

$$\mathbf{k}_p = \mathbf{k}_a + \mathbf{k}_b \quad (1b)$$

In our experiment we used Type I SPDC, where the daughter photons have the same polarisation.

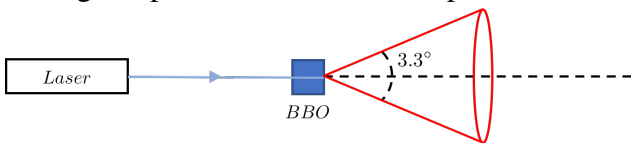


Figure 1: Schematic representation of SPDC

The quantum state of the two daughter photons after the SPDC is given by [\[7\]](#):

$$|\psi_{SPDC}\rangle = \int d\omega_a \int d\omega_b f(\omega_a, \omega_b) \alpha(\omega_a, \omega_b) \times \hat{a}_1^\dagger(\omega_a) \hat{a}_2^\dagger(\omega_b) |0\rangle, \quad (2)$$

with $\omega_{a,b,p}$ frequencies and $\hat{a}_1^\dagger(\omega_a), \hat{a}_2^\dagger(\omega_b)$ creation operators for photons with frequencies ω_a, ω_b . The function α is often called the “pump envelope function” [\[7\]](#). The frequency distribution for the two photons is given by $f(\omega_a, \omega_b)$ and $|0\rangle$ is the vacuum state. We will be considering Type I SPDC and narrow band pump from which it can be argued [\[8\]](#) that the pump envelope function takes the form of $\alpha(\omega_a, \omega_b) = \delta(\omega_a + \omega_b - \omega_p)$. Defining $\omega' = \omega_a - \frac{\omega_p}{2}$ and using the Dirac delta function (δ) to simplify the state [Eq. 2](#) we obtain:

$$|\psi_{SPDC}\rangle = \int d\omega' f'(\omega') \hat{a}_1^\dagger\left(\frac{\omega_p}{2} + \omega'\right) \times \hat{a}_2^\dagger\left(\frac{\omega_p}{2} - \omega'\right) |0\rangle. \quad (3)$$

2.2 Path Difference and Beam Splitter

The photons after SPDC are considered to be indistinguishable, so in order to add a degree of distinguishability, we can add a delay in one of the photon paths. Such a delay in path 2 can be written as $\hat{a}_2^\dagger(\omega) \rightarrow \hat{a}_2^\dagger(\omega) e^{-i\omega\tau}$, where τ represents the time-delay added in path 2 (so the path-difference is actually $c\tau$) [\[9\]](#). The state in [Eq. 3](#) then changes to [\[7\]](#):

$$|\psi_{PD}(\tau)\rangle = \int d\omega' f'(\omega') \hat{a}_1^\dagger\left(\frac{\omega_p}{2} + \omega'\right) \times \hat{a}_2^\dagger\left(\frac{\omega_p}{2} - \omega'\right) e^{-i(\frac{\omega_p}{2} - \omega')\tau} |0\rangle. \quad (4)$$

We now consider these two daughter photons as inputs of a 50:50 beam splitter which leads to the four possible outcomes depicted in [Fig. 2](#).

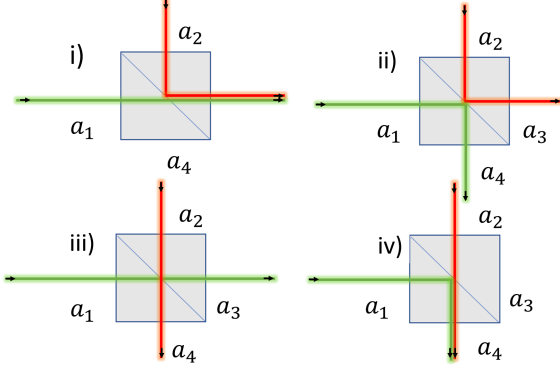


Figure 2: The possible outcomes of two photons (red and green) interacting within a 50:50 beam splitter: i) red beam reflects while green transmits; ii) both red and green beams reflect; iii) both beams transmit; and iv) red transmits while green reflects.

The action of a beam splitter on the creation operators in Eq. 3 is given by [9]:

$$\hat{a}_1^\dagger(\omega) \rightarrow \frac{1}{\sqrt{2}} \left(i\hat{a}_3^\dagger(\omega) + \hat{a}_4^\dagger(\omega) \right), \quad (5)$$

$$\hat{a}_2^\dagger(\omega) \rightarrow \frac{1}{\sqrt{2}} \left(\hat{a}_3^\dagger(\omega) + i\hat{a}_4^\dagger(\omega) \right), \quad (6)$$

and therefore, the state after the beam splitter is:

$$\begin{aligned} |\psi_{out}(\tau)\rangle = & \frac{1}{2} \int d\omega' f'(\omega') \\ & \times \left[i\hat{a}_3^\dagger\left(\frac{\omega_p}{2} + \omega'\right) + \hat{a}_4^\dagger\left(\frac{\omega_p}{2} + \omega'\right) \right] \\ & \times \left[\hat{a}_3^\dagger\left(\frac{\omega_p}{2} - \omega'\right) + i\hat{a}_4^\dagger\left(\frac{\omega_p}{2} - \omega'\right) \right] \\ & \times e^{-i\left(\frac{\omega_p}{2} - \omega'\right)\tau} |0\rangle. \end{aligned} \quad (7)$$

2.3 Probability of Coincidences

We are now interested in cases ii) and iv) in Fig. 2 which represent the cases where we will obtain a coincidence measurement in detectors placed at the outputs of the beam splitter. These detectors in paths a_3 and a_4 can be modelled as the measurements operators \hat{M}_3 and \hat{M}_4 acting as [10]:

$$\hat{M}_i = \int d\omega \hat{a}_i^\dagger(\omega) |0\rangle \langle 0| \hat{a}_i(\omega), \quad i \in \{3, 4\}. \quad (8)$$

The probability of obtaining coincidences in the detectors is therefore given by [10]:

$$p_{34}(\tau) = \langle \psi_{out}(\tau) | \hat{M}_3 \otimes \hat{M}_4 | \psi_{out}(\tau) \rangle. \quad (9)$$

Putting measurements (Eq. 8) and our state (Eq. 7) into Eq. 9 and performing the calculation we get:

$$p_{34}(\tau) = \frac{1}{4} \int d\omega' |f'(\omega')|^2 \left(2 - e^{-i2\omega'\tau} - e^{i2\omega'\tau} \right). \quad (10)$$

This equation gives the probability of coincidences at detectors placed at the outputs of a beam splitter as a function of the path difference (τ) between the two down converted photons and the function modelling their frequency distribution.

The shape of this probability of coincidences (Eq. 10) is strongly dependent on the frequency distribution of the down-converted photons $f'(\omega')$ which is experimentally determined by the type of bandpass filters used in the laboratory. Here we will address two of the most common options, Gaussian and Top-Hat functions given by:

$$f'_G(\omega') = C_G \frac{e^{-\frac{(\omega' - \omega_p)^2}{4\sigma^2}}}{4\sigma^2}, \quad (11)$$

$$f'_{TH}(\omega') = C_{TH} \begin{cases} 1 & \text{if } \omega_0 - \Delta\omega \leq \omega' \leq \omega_0 + \Delta\omega, \\ 0 & \text{otherwise,} \end{cases} \quad (12)$$

where C_G and C_{TH} are normalisation constants, σ and $\Delta\omega$ is the bandwidth. In Fig. 3 and Fig. 4 we have plotted the probability of coincidences (Eq. 10) when considering these two options Eq. 11 and Eq. 12 respectively.

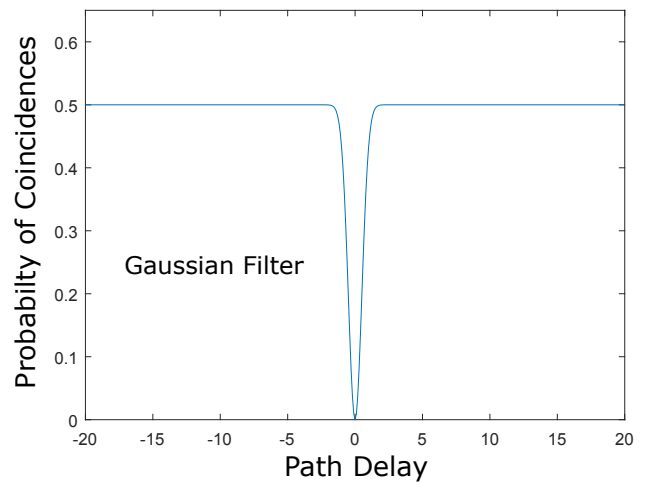


Figure 3: Expected behaviour of the probability of coincidences (Eq. 10) as a function of the path delay (dimensionless units) when considering bandpass filters modelled as the Gaussian function (Eq. 11).

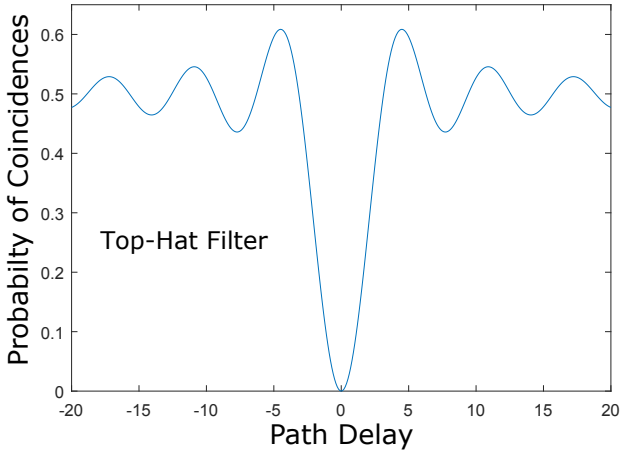


Figure 4: Expected behaviour of the probability of coincidences (Eq. 10) as a function of the path delay (dimensionless units) when considering bandpass filters modelled as the Top-hat function (Eq. 12).

From both cases Fig. 3 and Fig. 4, we have that the probability of coincidences presents a “dip” when approaching zero-delay, which is the HOM dip. The two photons become distinguishable when consider-

ing a path delay between them and the probability of coincidences is non-zero. The probability tends to 0.5 for large values of τ . Finally, we can also see that when considering the Top-Hat function we get rippled edges in the dip.

We have then, that the shape of the probability of coincidences is indeed strongly dependant on the frequency distribution of the down converted photons which in turn, can be experimentally adjusted in the laboratory by means of bandpass filters. The bandpass filters available in our laboratory can be considerably well modelled by a Top-Hat function (see section 6 for a transmission vs wavelength plot) and therefore, we were expecting to get a rippled HOM dip from our experimental setup, which we are going to fully detail in what follows.

3 Experimental Method

This section covers the equipment used and a detailed description of the experimental procedure, from aligning the pump laser to data processing.

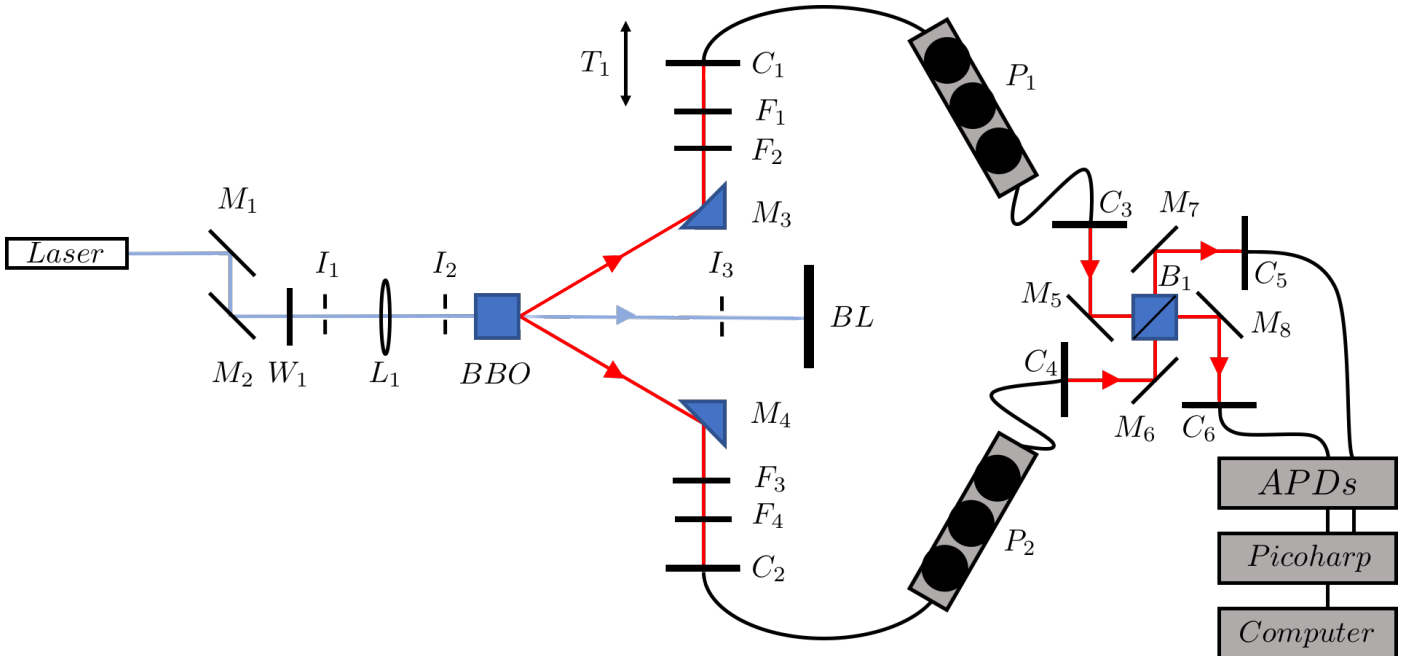


Figure 5: Experimental arrangement used. Equipment is labelled according to the following convention: M = mirror; W = waveplate; I = iris; L = lens; BL = beam block; P = polarisation paddles; F = filters; C = fibre couplers; and B = Beam splitter.

3.1 Cleaning

All the optical surfaces such as: mirrors, beam splitters, prisms, lenses, filters were cleaned before setting up the experiment. During the course of the experiment any optical surfaces which became dirty (by being touched inadvertently or by becoming dusty) were cleaned as necessary.

To clean an optical surface, first the component is removed from its mount to allow greater access to the surface. The surface is then cleaned by applying a few drops of methanol to soft tissue paper and wiping across the surface in a single direction.

3.2 Preparation

The experimental setup is illustrated in Fig. 5. The optical elements were roughly put in the correct position before fine alignment began. This was done to ensure the fibres reached and so that there was enough room on the optical table.

The two limiting parameters in the experiment were the focal length of the lens and the walk-off angle of the BBO crystal. The first corresponds to L_1 on Fig. 5, which was 20 cm (the focal length of the lens). The BBO-to-prism distance was calculated to be 16 cm in order to minimise scatter from the pump laser using the walk-off angle.

The path difference of the daughter photons was measured to be equal for the two arms of the experiment within ± 1 cm.

3.3 Aligning the pump

A Toptica iBeam-405_00029 405 nm continuous wave laser was used to pump the BBO crystal in this experiment. The power of the laser could be controlled via USB using a computer, up to a maximum of 180 mW. All alignment was performed at 3.0 mW, which was sufficiently high to easily see the beam. After mounting the laser, the beam was found to be 9.7 cm above the table. To ensure that the laser beam remained level throughout the experiment, two irises (I_2 and I_3) were set to 9.7 cm above the table and placed along a row of holes. Two mirrors (M_1 and M_2) were used to align the laser beam through the two irises. The alignment was optimized by placing a power meter after the second iris and

making fine adjustments to the mirrors to maximize the power reading.

After placing the waveplate W_1 and the BBO (between I_2 and I_3) in the path of the beam, the laser was re-aligned to maximise the power through the irises. Then a third iris (I_1) and a lens with a focal length of 20 cm were placed between the waveplate and iris 2. The lens was finely adjusted such that the reflected spot on iris 1 coincided with the incoming laser beam through iris 1. The lens and BBO were both mounted on translation stages along the optical axis. The first translation stage was used to focus the beam in the crystal (by setting 20 cm between the lens and the BBO).

3.4 Polarization

A polarizing beam splitter (PBS), shown in Fig. 6 was used to measure the power at each of the detector spots A_1 and A_2 . A $\lambda/2$ wave plate at 45° was used to rotate the polarization of the pump beam until all of the pump was transmitted through the PBS. Only a $\lambda/2$ wave plate was needed as the pump was linearly polarized.

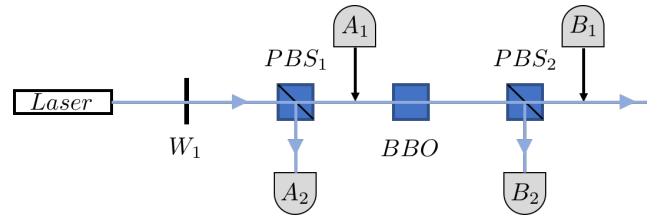


Figure 6: Procedure used to set the waveplates so that the pump laser was fully transmitted through the PBS and then to align the orientation of the BBO with the optical axis.

The BBO was aligned using a PBS as above with detectors now at B_1 and B_2 , rotating the crystal until the polarization of the pump laser did not change when passing through the crystal. The BBO had two different orientations, 0° and 90° where only the 90° orientation produced SPDC.

3.5 Spontaneous Parametric Down Conversion

To accurately collect SPDC photon pairs generated by the nonlinear crystal, calculations were first carried out in order to ascertain the optimum separation of the reflecting prisms. Their distances from the crystal were chosen so that the pump laser would pass through the middle of the prisms into a beam blocker, whilst still enabling the reflection of SPDC photons into the fibre coupler aligners (C_1, C_2). The pump beam diameter was ≈ 5 mm, thus it was decided that the prism separation should be ≈ 7 mm. Knowing the separation, and the angle at which SPDC photons were generated from the crystal (3.3°), the prisms were placed ≈ 16 cm apart from one another, calculated via simple trigonometric principles.

C_1 and C_2 were both mounted onto x, y, z translation stages so that coarse alignment could be carried out in three dimensions. The x -translation stage of C_1 was motorised such that this degree of freedom could be controlled with a computer program, whilst that of C_2 was manual.

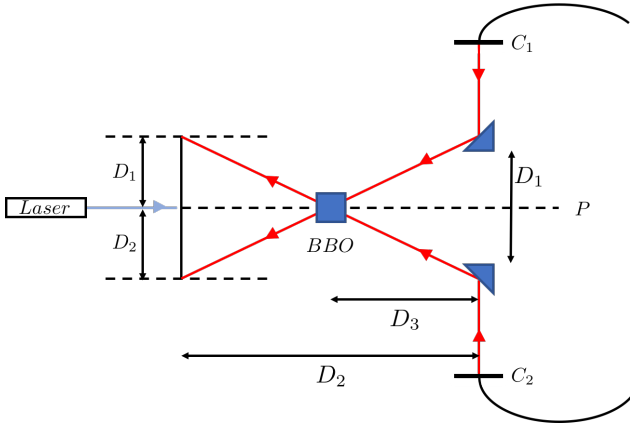


Figure 7: Back aligning

Coarse back alignment, shown in Fig. 7 was achieved utilising a guide laser (632 nm). Before trying to back align through the prisms, the beams were first levelled using height sticks and set to the height of the pump laser using the z -translation stage on C_1 and C_2 . Their lenses were then focused to produce collimated beams, and the tilt on both prisms was also zeroed by resetting the tilt adjustment knobs. Once all of this had been achieved, the back align-

ing lasers were passed onto the prisms and reflected into the BBO.

Fine back alignment was achieved via a two step iterative process. Initially, the beams were adjusted using the x, y, z translation stages on C_1 and C_2 so that both beams passed through the same point in BBO as the pump laser. Secondly, the points at which the back aligning lasers should hit a beam card after they had passed through the BBO was determined by trigonometry. The x -translation stages on C_1 and C_2 were then moved to compensate for with prism rotation so that the beams hit the correct points.

Next, the back aligning lasers were removed and C_1 and C_2 were connected to the APD interface and PicoHarp detection hardware, so that single photon coincidence counts could be detected. Via the iterative adjustment of both the y - and z -translation stages on C_1 and C_2 the focal length knob, coincidence counts were maximised. Finally, UV and IR filters F_1, F_2, F_3, F_4 were introduced and optimisation of coincidence counts was achieved by tilting the BBO. The UV filters (F_2, F_3) protected the APDs from scattered laser light, and the IR filters were used to refine the spectrum of the SPDC photons.

3.6 The Interferometer

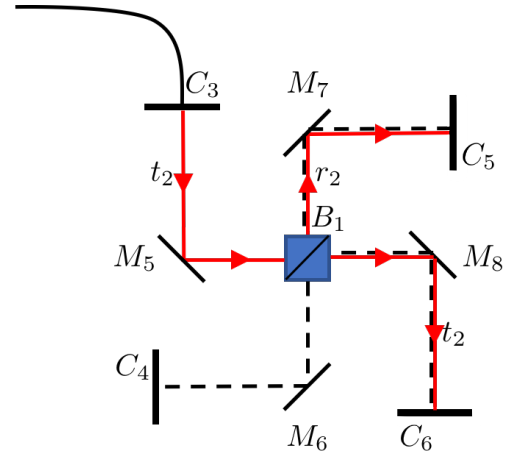


Figure 8: Procedure for aligning the HOM interferometer

The interferometer, Fig. 8, was constructed using four fibre couplers, four mirrors and a beam splitter. The fibre couplers (F220FC-780) were designed

for 780 nm, but operate sufficiently well with 810 nm light.

In general, alignment of a path through the interferometer involved two steps: shining two lasers in opposite directions through the path, and ensuring that the beams overlap at all points (back-aligning); and then shining a single 810 nm laser into the input and maximising the power at the output using a fibre coupled power meter.

The alignment process for the interferometer relies on the principle that the transmitted mode through a beam splitter is unchanged by minor modifications in the orientation of the beam splitter. This meant that the light from C_4 could be coupled into C_5 by changing M_6 , M_7 and C_5 , without considering the position of the beam splitter. Then the reflected mode was aligned by changing M_8 , C_6 and the beam splitter orientation.

After the first input to the beam splitter was aligned to its transmitted and reflected paths the procedure for aligning the second input was simplified. To ensure the mode overlap between the two daughter photons the second input (C_3) was coupled to its transmitted path. This guaranteed that the second input in its reflected path was also fibre coupled. Once both outputs were coupled it meant that both the inputs overlapped everywhere after the beam splitter and therefore overlap in the beam splitter.

3.7 Path Difference and Polarization Control

The fibre coupler aligner C_1 was mounted on the electronic SMC100-C translation stage along T_1 , with a range of 50 mm, which was controlled via the computer. The paths from the prisms to each fibre coupler and beam splitter (M_3 to B_1 and M_4 to B_1) were adjusted to be the same. The estimated error in the zero path difference measurement was ± 1 cm.

The width of the dip was calculated using $\lambda^2/\Delta\lambda$ [11] to be $\sim 65 \mu\text{m}$. This equation could be derived, in principle, from analytically addressing the probability of coincidences addressed in Eq. 9. Using this value the stage was moved at $5 \mu\text{m/s}$ so that the dip in coincidences would be visible for ~ 10 s. The ± 1 cm scanning range was split into four 5 mm sections each taking 17 minutes to scan through.

Two FPC560 fibre paddles P_1, P_2 were used to control the polarization of the signal and idlers with 2-3-2 winds. This was done in order to maximise the visibility of the dip by making sure the daughter photons had the same polarization at the beam splitter. Using the PBS technique in subsection 3.4 above the paddles were separately positioned to maximise transmission into the fibre couplers after the interferometer.

As the fibre coupler aligner moved on the translation stage (along T_1), it became decoupled. Once the dip was found the fibre coupler was re-coupled to maximise coincidences at the HOM dip. For the final data steps of $2 \mu\text{m}$ were used from 28.70 mm to 29.00 mm giving 152 readings.

3.8 UV and IR filters

As discussed in subsection 2.3 the width and shape of the dip is related to the Fourier transform of the filters used. For each fibre coupler aligner a long pass UV filter was used to block the majority of the pump scatter and an 810 nm/10 nm narrow band filter, Fig. 13. The relationship between the filters and the dip was also investigated with results presented in the appendix.

3.9 APDs and Coincidence Counting

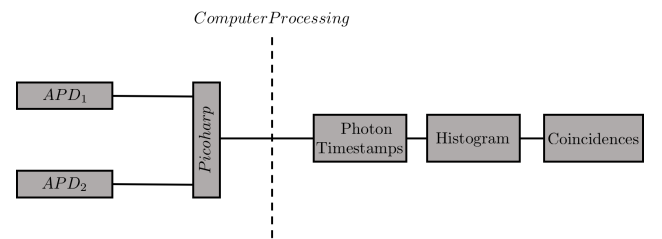


Figure 9: Processing of the signal from the APDs

An Avalanche Photodiode (APD) was connected to a PicoHarp 300 time tagger Fig. 9 which has a resolution of 4 ps. The PicoHarp has an input voltage range of 0 to -1 V, therefore the APD which outputs TTL signals had to be connected via a PicoQuant SIA 400 – an inverter and attenuator module, resulting in -2 V pulses. The Constant Fraction Discriminator (CFD) levels of the PicoHarp channels were

then set to the maximum of 800 mV to ensure that the amount of noise was minimised.

The PicoHarp has several modes of operation – two of which were useful in this experiment. The first was Oscilloscope mode which displayed live counts for the number of photons in each channel and a histogram of the time between photons arriving at channel 0 and then at 1. This mode was set to have a refresh rate of 1 s – in order to average out noise – which was useful for checking if SPDC had been achieved and for fine alignment purposes in real time. The other useful mode was T2 mode, this is a type of Time-Tagged Time-Resolved (TTTR) mode [12] which records the arrival time and channel of each photon. This allowed for a more detailed analysis of the data and so was used for the final measurements.

Once SPDC was achieved there were two things to determine: which channels of the APD to use for measurements; and what the coincidence time window should be. The APD has 4 channels each with different noise levels and time delays. After some investigation using Oscilloscope mode, channel 1 and 2 were found to be the best as coincidences were peaked around 1 ns as seen in the Fig. 10. This meant that setting the time window to 2.5 ns would ensure that all the actual coincidences were accounted for and the accidentals minimised.

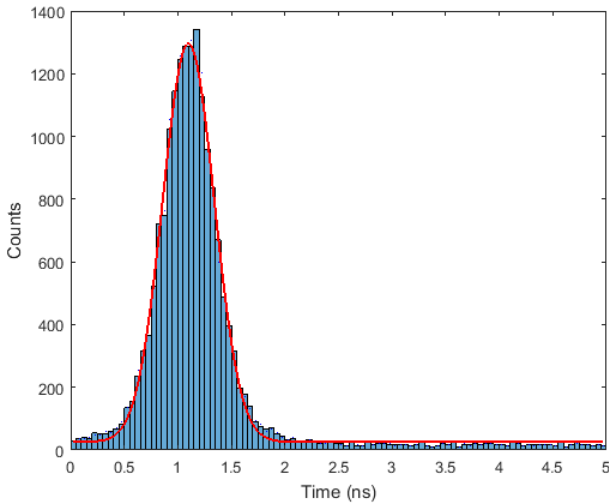


Figure 10: Histogram of time delay between consecutive photons from SPDC in a 5 ns window with a fitted Gaussian. APD channels 1 and 2.

All data processing was carried out in MATLAB.

The output of a T2 mode measurement was a binary file (.ptu) which needed to be converted into a readable format. Demo code *Read_PTU.m* that was provided with the PicoHarp software was modified to make this process more efficient. Code also had to be written to calculate the number of coincidences. Since the PicoHarp has a dead-time of 90 ns on each channel and none across the two channels, this code simply looked at whether two consecutive photons arrived at different channels and if their time delay was within the coincidence window.

Accidental coincidences are considered to be those coincidences which did not result from SPDC pairs. Accidentals were calculated by looking at how many coincidences fall outside of the 2.5 ns time window. The number of coincidences in 3-10 ns were calculated and averaged to find the average number of accidentals for each measurement. As the figures in section 4 will show, the number of accidentals stayed steady for each dip.

4 Results

Each full measurement of the dip consisted of between 70-150 1 second T2 measurements taken consecutively at 2 μm intervals at a pump power of 50 mW. Several of these detailed run-throughs of the dip were done over the space of a few days. Since the baseline number of coincidences fluctuated from day to day due to decoupling and other factors, the figures below have different scales and visibilities. The visibility is calculated by taking the minimum number of coincidences away from the baseline number of coincidences and dividing by their sum.

$$\text{Visibility} = \frac{\text{Baseline} - \text{Minimum}}{\text{Baseline} + \text{Minimum}} \quad (13)$$

Fig. 11 is a plot of the first dip measured. The key properties of this dip are the $91.9 \pm 0.5\%$ visibility once accidentals are taken into account and width of 63.4 μm when measuring from the maximums. Another feature to note is the ripple at the top of the dip, this is a result of the profile of the bandpass filters (as mentioned in subsection 2.3). To investigate this ripple further, the next dip measurement Fig. 12 started and ended further away from the centre of the dip.

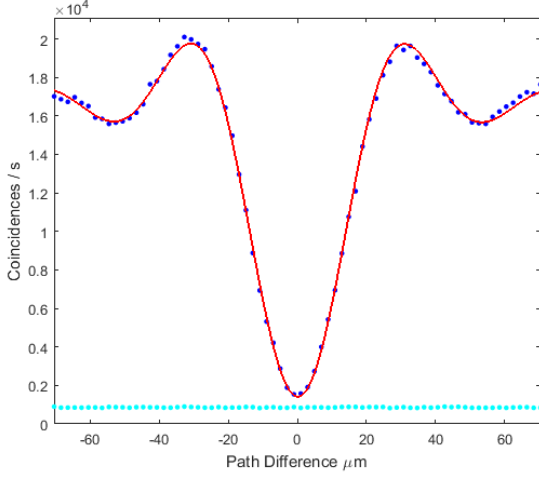


Figure 11: HOM Dip with a visibility of $91.9 \pm 0.5\%$. 8.4×10^5 singles/s and baseline 1.7×10^4 coincidences/s and average accidentals of 857. The blue dots represent the data [13], the red line the fitted curve and light blue dots the accidentals.

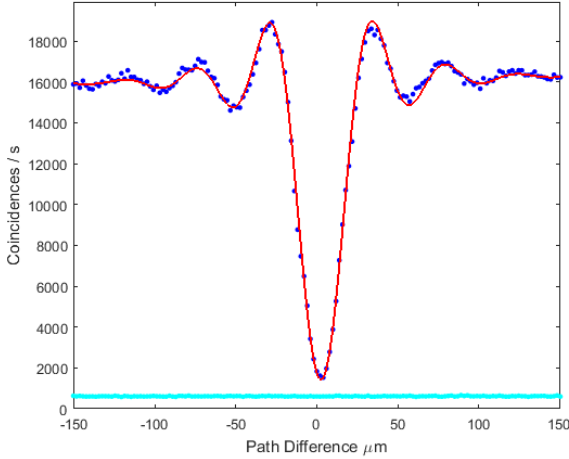


Figure 12: Investigation of the ripples, HOM Dip with a visibility of $88.8 \pm 0.1\%$. 7.1×10^5 singles/s, baseline of 1.6×10^4 coincidences/s and average accidentals of 612.

The fitted curve Eq. 14 is a function that consists of a Gaussian term to account for the wavepacket of the photons, a Sinc term to account for the Top-Hat profile of the bandpass filters and a linear term to deal with any decoupling [14]. The fitted curve as a function of path difference x is therefore,

$$(c_1x + c_2) \left[1 - \text{sinc}(c_3(x - c_4))e^{c_5(x - c_4)^2} \right] + c_6. \quad (14)$$

5 Discussion

The results are now compared to other published work. Visibilities and coupling efficiencies between different experimental setups are compared. Errors in the experiment and possible improvements are discussed.

5.1 HOM Dip Profile

The exact shape of the HOM dip arises from the phase matching condition in the BBO and the frequency response of the filters. As described above, the BBO produces two beams of light with frequencies ω_a and ω_b satisfying

$$\omega_a + \omega_b = \omega_p. \quad (15)$$

The wave vectors of the beams are then related by

$$\mathbf{k}_p = \mathbf{k}_a + \mathbf{k}_b + \Delta\mathbf{k}, \quad (16)$$

where \mathbf{k}_p is the wave vector of the pump source. When $\Delta\mathbf{k} = 0$ the phase matching condition Eq. 1b is satisfied and the signal and idler beam intensities are maximised. As the magnitude of $\Delta\mathbf{k}$ increases, the intensities of the daughter beams decrease. The position of C_1 and C_2 fixes particular choices of \mathbf{k}_a and \mathbf{k}_b . There are then a range of frequencies ω_a and ω_b satisfying Eq. 15 which are coupled to C_1 and C_2 , with associated intensities depending on the size of $\Delta\mathbf{k}$ in each case. Hence the light coupled into C_1 and C_2 has a particular spectrum which is peaked at the centre frequency $\omega_p/2$ and falls off smoothly depending on the properties of the nonlinear crystal. The spectrum can be modified by placing a filter in the path of the signal and idler beams, which determines the precise shape of the HOM dip, as described in the theory section above.

5.2 Properties of the photon pair source

Typical visibilities for HOM dips using bulk optical elements are 89% and 91% [15]. Other methods of obtaining a HOM dip resulted in observed visibilities of 80% [3] (bulk optics), 82.9% [16] (fibre optics) and 98.2% [5] (integrated optics). Two independently prepared photons using a Lithium niobate

waveguide achieved $87 \pm 4\%$ [17] in a pulsed integrated setup.

The visibilities of 91.9% in Fig. 11 and 88.6% in Fig. 12 both show that a non-classical correlation was observed as visibility $> 50\%$ [18].

The coincidence efficiency is calculated by taking the ratio of coincidences to single counts. Fig. 11 had a ratio of 2.0%. After increasing the path difference range, Fig. 12 had a coincidence to single ratio of 2.3%.

The coincidence to accidental coincidence ratio for the two cases were Fig. 11 had a ratio of 19.8 coincidences to accidentals. Extending to a larger path difference, Fig. 12 had a ratio of 26.1 coincidences to accidentals.

These values are comparable to [19] who reported a coincidence to single ratio of 4.7% and the coincidence to accidental ratio was much higher than than their reported value of 2.68.

5.3 Width of PicoHarp peak

A histogram of the arrival times for the photons at one particular position of C_1 is shown in Fig. 10. The vast majority of counts fall in the range 0 to 2.5 ns, with a Gaussian distribution centred on 1 ns. Since light would travel 0.3 m in 1 ns, which is significantly longer than the path difference in the experiment, this displaced peak is due to delays in the detector electronics. This was verified by swapping the PicoHarp channels, which caused shifts in the peak of the Gaussian on the order of 1 ns. The Gaussian itself is due to the jitter of the APDs, which is a measure of the uncertainty in the difference between the time of arrival of the photon and the time of the output pulse of the APD.

5.4 Sources of Error

There are several sources of error that did not allow for exact replications of the experiment. This made it difficult to determine what the errors in the measurement of coincidences are and to fit error bars to the plots of the HOM Dip.

For example, the electronic translation stage does not go back to the same positions with every run-through of the experiment due to the way the motion

controller is constructed. In addition, from day to day the components of the experiment can become less aligned, whether it is from gravity shifting the fibre coupler aligners, C_1 and C_2 , downwards or vibrations and accidental movements of the table.

Care was taken to return any micrometers to their recorded positions and re-align for maximum coincidences whenever a full measurement of the dip was taken. However, it was not always possible to achieve this and get the same visibility for every measured dip.

5.5 Improvements

There are several changes which could be made to the experiment either to improve the results or to make the experiment easier to conduct. The experiment could be conducted more easily by using polarisation maintaining fibres connected to a fibre beam splitter. The fibres would remove the need to optimise the polarisation of the SPDC photons, and the fibre beam splitter would remove the need to align several mirrors and fibre couplers. In addition to saving time this would reduce loss and noise in the interferometer and improve the polarisation agreement between the two SPDC photons, both of which would improve the visibility of the HOM dip.

The data collection process would be simplified by using equipment intended specifically for coincidence counting (the PicoHarp is intended primarily for use in fluorescence spectroscopy). This might remove the need to manually count coincidences from files containing photon time stamps.

As described above, the automated translation stage suffered from hysteresis which compromised repeated measurements. Improving the accuracy and repeatability of the translation stage would improve the quality of the data.

The experiment would be improved significantly by automating the data collection process. This would remove the lengthy and error prone process of manually setting the translation stage and then manually collecting photon time stamp data. In addition, the process could then be performed in total darkness without anyone in the vicinity of the experiment.

It has been shown that pump power effects the visibility of the HOM dip [20], due to a trade-off

between the level of SPDC and noise in the single counts. The experiment could be further improved by repeating the data collection process for different pump powers in order to characterise the resulting changes in visibility.

6 Conclusion

In conclusion, we have demonstrated HOM interference dip of width $63.4\mu\text{m}$ and visibilities between 88.8-91.9% using an arrangement of bulk optical elements as outlined in Fig. 5. These visibility measurements compare favourably to those observed in the original discovery of the effect, where the obtained visibility was 88% over a width of around $16\mu\text{m}$ at half height.

References

- [1] C. K. Hong, Z. Y. Ou, and L. Mandel, "Measurement of subpicosecond time intervals between two photons by interference," *Phys. Rev. Lett.*, vol. 59, pp. 2044–2046, Nov 1987.
- [2] E. Knill, R. Laflamme, and G. J. Milburn, "A scheme for efficient quantum computation with linear optics," *nature*, vol. 409, no. 6816, pp. 46–52, 2001.
- [3] J. G. Rarity and P. Tapster, "Fourth-order interference in parametric downconversion," *JOSA B*, vol. 6, no. 6, pp. 1221–1226, 1989.
- [4] A. Ourjoumtsev, M.-C. Dheur, T. Avignon, and L. Jacubowicz, "Two-photon quantum interference for an undergraduate lab," *European Journal of Physics*, vol. 36, no. 6, p. 065034, 2015.
- [5] J. C. F. Matthews, A. Politi, A. Stefanov, and J. L. O'Brien, "Manipulation of multiphoton entanglement in waveguide quantum circuits," *Nature Photonics*, vol. 3, no. 6, pp. 346–350, 2009.
- [6] A. Thoma, P. Schnauber, M. Gschrey, M. Seifried, J. Wolters, J. H. Schulze, A. Strittmatter, S. Rodt, A. Carmele, A. Knorr, T. Heindel, and S. Reitzenstein, "Exploring Dephasing of a Solid-State Quantum Emitter via Time- and Temperature-Dependent Hong-Ou-Mandel Experiments," *Physical Review Letters*, vol. 116, no. 3, 2016.
- [7] A. M. Brańczyk, A. Fedrizzi, T. M. Stace, T. C. Ralph, and A. G. White, "Engineered optical nonlinearity for quantum light sources," *Opt. Express*, vol. 19, pp. 55–65, Jan 2011.
- [8] Z. Ou, *Multi-Photon Quantum Interference*. Springer US, 2007.
- [9] C. Gerry and P. Knight, *Introductory Quantum Optics*. Cambridge University Press, 2005.
- [10] A. M. Brańczyk, T. C. Ralph, W. Helwig, and C. Silberhorn, "Optimized generation of heralded fock states using parametric down-conversion," *New Journal of Physics*, vol. 12, no. 6, p. 063001, 2010.
- [11] H. Li, S. Przeslak, A. Niskanen, J. Matthews, A. Politi, P. Shadbolt, A. Laing, M. Lobino, M. Thompson, and J. O'Brien, "Reconfigurable controlled two-qubit operation on a quantum photonic chip," *New Journal of Physics*, vol. 13, no. 11, p. 115009, 2011.
- [12] PicoQuant, "PicoHarp 300 User's Manual and Technical Data - Software version 3.0.0.3," 2015.
- [13] <https://github.com/ot561/homdip>.
- [14] P. Shadbolt, *Complexity and Control in Quantum Photonics*. Springer Theses, Springer International Publishing, 2016.
- [15] R. Okamoto, J. O'Brien, H. Hofmann, and S. Takeuchi, "Realization of a Knill-Laflamme-Milburn C-NOT gate—a photonic quantum circuit combining effective optical nonlinearities," 2010. Available at: <https://arxiv.org/abs/1006.4743>.
- [16] Z. Zhou, Y. Li, Z. Xu, S. Wang, L. Xu, B. Shi, and G. Guo, "Hong-Ou-Mandel interference between two independent all fiber photon sources," 2016. Available at: <https://arxiv.org/abs/1607.02301>.

- [17] Y. Tsujimoto, Y. Sugiura, M. Tanaka, R. Ikuta, S. Miki, T. Yamashita, H. Terai, M. Fujiwara, T. Yamamoto, M. Koashi, *et al.*, “High visibility hong-ou-mandel interference via a time-resolved coincidence measurement,” *Optics Express*, vol. 25, no. 11, pp. 12069–12080, 2017.
- [18] R. Ghosh and L. Mandel, “Observation of non-classical effects in the interference of two photons,” *Physical Review Letters*, vol. 59, no. 17, p. 1903, 1987.
- [19] H. Kim, S. M. Lee, and H. S. Moon, “Generalized quantum interference of correlated photon pairs,” *Scientific reports*, vol. 5, p. 9931, 2015.
- [20] T. Kobayashi, R. Ikuta, S. Yasui, S. Miki, T. Yamashita, H. Terai, T. Yamamoto, M. Koashi, and N. Imoto, “Frequency-domain hong-ou-mandel interference,” *Nature Photonics*, vol. 10, no. 7, pp. 441–444, 2016.
- [21] http://www.laser2000.co.uk/semrock_filter.php?code=FF01-810/10-25.

Appendices

A. Top-Hat bandpass filters

The bandpass filters that were available to us in the lab were two brightline fluorescence filters 810/10 [21]. In Fig. 13, we have plotted the transmission of these filters vs wavelength with the information available from their webpage, which let us assume that we can indeed model these filters as the Top-Hat function in Eq. 12, and therefore we would be expecting a rippled HOM dip as in Fig. 4.

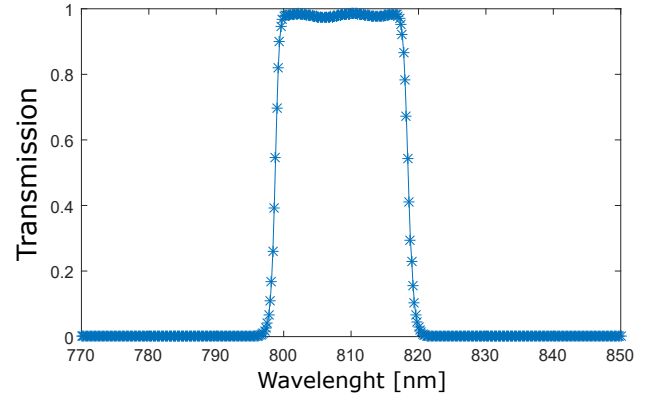


Figure 13: Transmission vs wavelength of the light through the bandpass filters available in our lab, BrightLine® single-band bandpass filter 810/10 nm [21].

B. HOM Dip with no bandpass filters

In Fig. 14, we investigated the interference with no Infra-red narrow band filters. This dip has a visibility of 49.4% with a width of 17.8 μm .

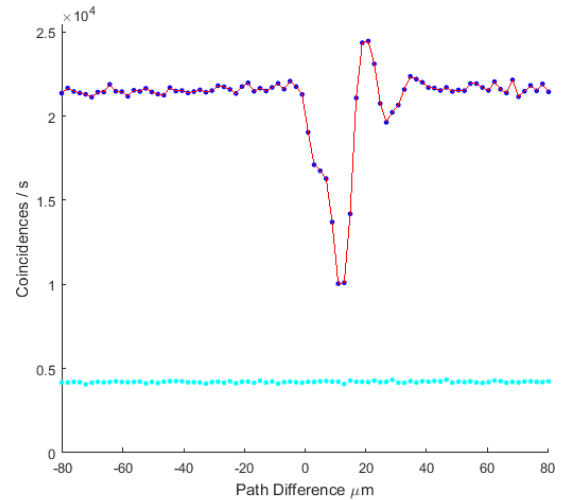


Figure 14: HOM Dip with both UV but no IR filters, pump power of 50 mW, 1.8×10^6 singles/s, baseline of 2.1×10^4 coincidences/s. Average accidentals of 4200. The blue dots represent the data, the red line to help guide the eye and light blue dots the accidentals.